CAAP Quarterly Report
December 30th, 2024

Project Name: Development of a Framework for Assessing Cathodic Protection (CP) Effectiveness in Pipelines Based on Artificial Intelligence (AI)

Contract Number: 693JK32350005CAAP

Prime University: ***Texas A&M Engineering Experiment Station***

Prepared By: PI Homero Castaneda-Lopez Professor, hcastaneda@tamu.edu,
phone: 9794589844

Reporting Period: October 1st – December 30th, 2024

Project Activities for Reporting Period:

Task 1. Designing and building the physical prototypes in laboratory conditions and deterministic modeling.

Mechanistic Numerical Analysis

Rather than using generic EEC values to represent the mechanisms that are occurring at the interface, it is possible to define the impedance response of specific mechanisms. These impedance definitions can then be used in the 2D TLM for modeling various processes. Initially, mechanistic analysis was performed for two cases: 1) an electrode that is coated with a coating that is capacitive, and 2) a simple one-step electrochemical reaction with no effects of external polarization or concentration gradients. Figure 1 depicts a general electrochemical interface for a coated samples immersed in an aqueous environment with various ions present, along with the EEC definitions of a coating that displays only capacitive and resistance + capacitive impedance response.

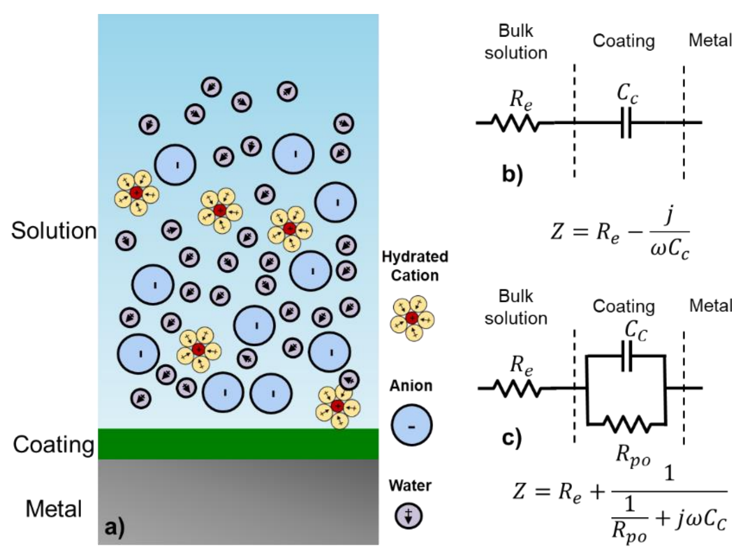

Figure 1: a) General electrochemical interface of a coated sample, b) EEC definition using only solution resistance and purely capacitive coating, and c) EEC definition using a solution resistance coupled to an imperfect coating that displays resistive and capacitive properties

For both cases in **Error! Reference source not found.**b and c the coating capacitive response was defined using the following equation:

$$C = \frac{\epsilon_0 \epsilon_r A}{d} \qquad (1)$$

Where ϵ_0 is the permittivity of free space, ϵ_r is the permittivity of the coating, A is the surface area, and d is the coatings thickness. ϵ_0 is a universal permittivity constant and does not change from system to system, and ϵ_r was determined experimentally from multiple electrochemical measurements. The value of ϵ_r was determined to be around 13.36 for a FBE coating. For each coating system the ϵ_r must either be found in literature or determined experimentally. The surface area was simply set as the total area that was exposed to the solution. The coating thickness was changed to various values to understand the effect of coating thickness on the impedance response of the system. Comparison of the impedance response of the EECs in Figure 1b and c are shown in **Error! Reference source not found.**.

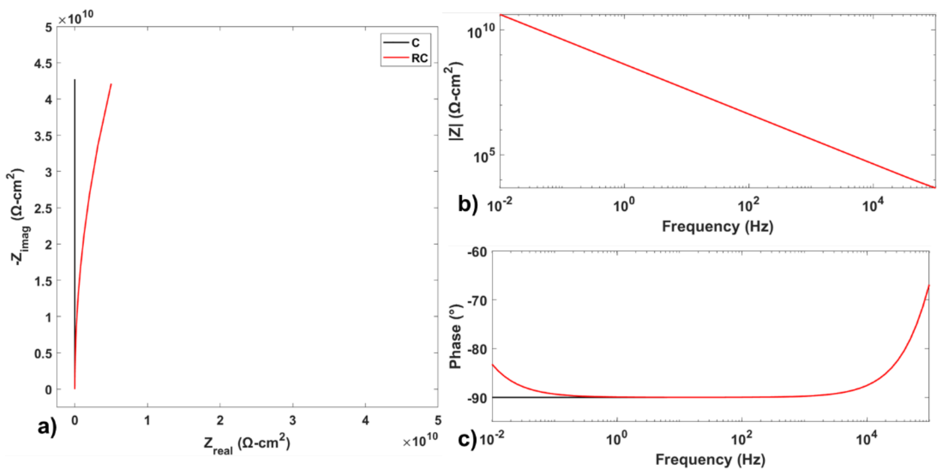

Figure 2: a) Nyquist, b) Bode, and c) Phase angle plots comparing a coating with a thickness of 1000 μm that display capacitive (black) and resistive + capacitive (red) response. Model Parameters: $\boldsymbol{Rs = 1.4\ k\Omega, R_{po} = 360 * 10^9 \Omega, \epsilon_r = 13.36, \epsilon_0 = 8.85 * 10^{-13} \frac{F}{m}, A = 3.1416 * 10^{-4}\ m^2, d = 100 * 10^{-6}\ m}$

It can be seen from Figure 2**Error! Reference source not found.** that for both EEC cases the overall impedance magnitude was the same over the entire frequency range. But in the two circuits deviate in the low frequency regime where the capacitive only EEC stayed around 90° over the frequency range of $10^{-2} - 10^{3}$ Hz. The resistive + capacitive EEC the deviation towards more positive phase angle values is due to the addition of the resistive component. In the low frequency regime $<10^{-1}$ Hz the preferred conduction path is through the resistive component of the circuit. The role of coating thickness on the impedance response of the system is shown in Figure 3. With increasing thickness, the overall impedance magnitude increases along with a change in the frequency response of the system.

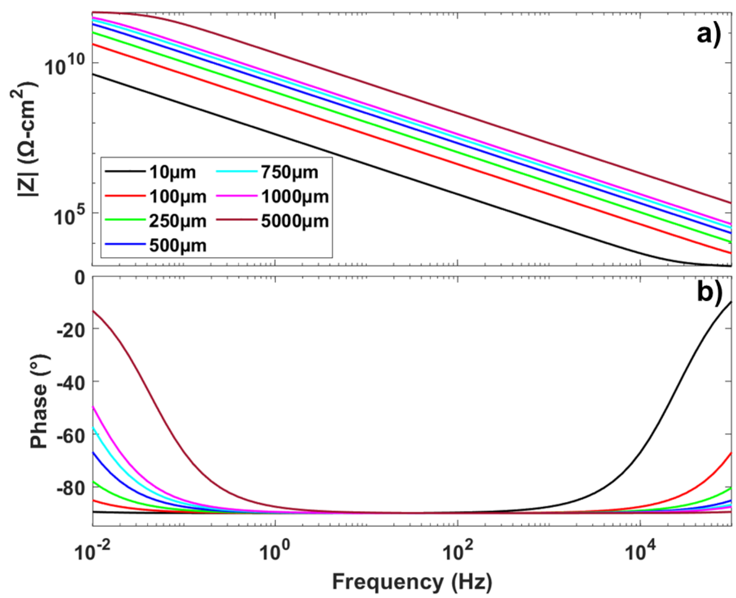

Figure 3: a) Bode and b) Phase angle plots showing the effect of coating thickness on the impedance response of the model

For case 2, Figure 4a and b depict a general electrochemical interface for a bare metal surface immersed in an aqueous environment with various ions present, along with the EEC definitions of the solution resistance and the general interfacial impedance. Figure 4c depicts the general interface impedance in terms of the faradaic and charging currents. Where the faradaic and charging currents are the portions of the current that are used in the charge transfer reaction and charging of the double layer respectively.

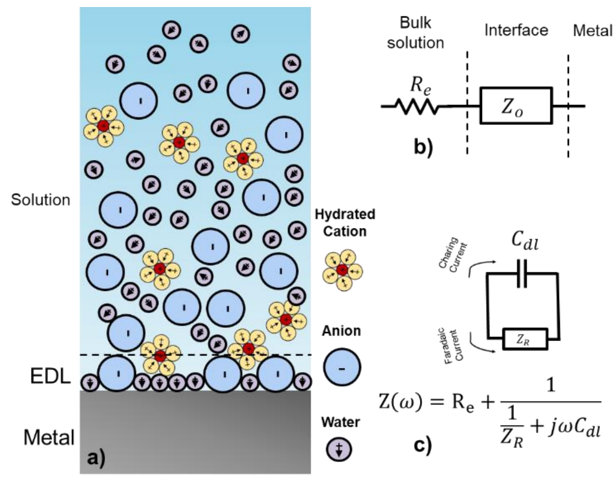

Figure 4: a) General electrochemical interface of a bare metal surface, b) EEC definition using only solution resistance and general interface impedance definition, and c) general impedance definition in terms of a charging and faradaic current

Equations 1 - 4 define the double layer capacitance and charge transfer resistance in terms of the electrochemical properties of the system.

$$C_{dl} = \left(\frac{1}{C_H} + \frac{1}{C_{diff}}\right) \qquad (2)$$

$$C_H = \frac{\epsilon A}{d} \tag{3}$$

$$C_{diff} = \left(\frac{n_0 \epsilon e_0^2}{2\pi k_B T}\right) \cosh\left(\frac{e_0 V}{2k_B T}\right) \tag{4}$$

$$R_{ct} = \frac{\tilde{V}}{\tilde{\imath}} = \frac{1}{\bar{\imath}\left(\frac{nF}{2RT}\right)} = \frac{1}{i_0 \cdot e^{\frac{nF}{2RT}\eta}\left(\frac{nF}{2RT}\right)} \tag{5}$$

For the double layer capacitance there were a few assumptions made for the initial derivation: no effect of ion adsorption, well mixed and homogenous solution, and only one ion predominantly playing a role in the corrosion process. C_H is defined as the Helmholtz capacitance, which is assumed to follow the same form as a flat plate capacitor where ϵ permittivity of water, A is the surface area, and d is the thickness of the layer which was assumed to be the radius of the solvated ions. C_{diff} is the capacitance of the diffuse layer, where ϵ permittivity of water, n_0 is the number of ions in the bulk solution, e_0 is the charge of the ion, V is the potential drop across the diffuse layer, k_B is the Boltzmann constant, and T is the temperature of the system. The total double layer capacitance is the combination of the Helmholtz capacitance and diffuse layer capacitance in series. There were two main assumptions made for the derivation for the charge transfer resistance: 1) only one reaction at the interface ($Fe \rightarrow Fe^{2+} + 2e^{-}$) and 2) the steady state current has the form of the following equation:

$$i = i_0 e^{\frac{nF}{2RT}\eta} \tag{6}$$

To define the charge transfer resistance the AC form of Ohm's law where it the sinusoidal potential divided by the sinusoidal current, which ends up being one over the steady state current times a constant. Where i_0 is the exchange current density of the reaction, n is the number of electrons transferred in the reaction, F is the Faraday Constant, R is the gas constant, and T is the temperature of the system. For the double layer capacitance and charge transfer resistance terms the parameter that was changed for each term was chloride concentration in the bulk solution and exchange current density respectively. The parameters used in the initial model are shown in Table 1and Table 2.

Table 1: Bases model parameters used to calculate the double layer capacitance

Parameter	Value
ϵ	6.903e-10
A	3.1423e-04
d	1.8100e-10
n_0	1.4720e+21
e_0	1.6024e-19
V	0.0250
k_B	1.3800e-23
T	298

Table 2: Base model parameters used to calculate the charge transfer resistance

Parameter	Value
i_0	1.2500e-06
n	2
F	9.6485e+04
R	8.3140
T	298

The role of chloride concentration and exchange current density are shown in Figure 5 and Figure 6. From Figure 5**Error! Reference source not found.** it can be seen that with increasing chloride concentration the overall capacitive response of the system decreases. This is most likely due to the increased bulk chloride concentration the overall length of the diffuse layer decreases creating a smaller and less capacitive double layer capacitance. Figure 6 shows that there is an inverse relationship between the exchange current density and the charge transfer resistance. Where increasing exchange current density will decrease the charge transfer resistance of the system. This logic makes sense, since with increasing exchange current density it would mean that the reaction is occurring faster at the interface which increase the overall corrosion current density of the system.

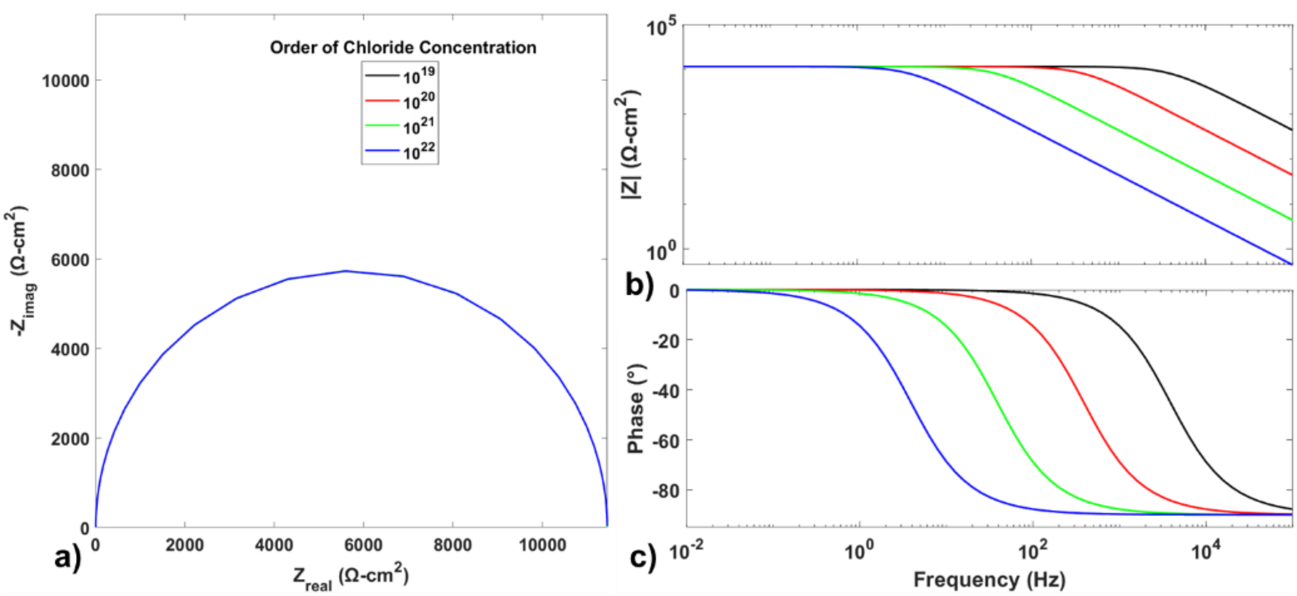

Figure 5: a) Nyquist, b) Bode, and c) Phase angle plots showing the role of bulk chloride concentration on the impedance response of the system

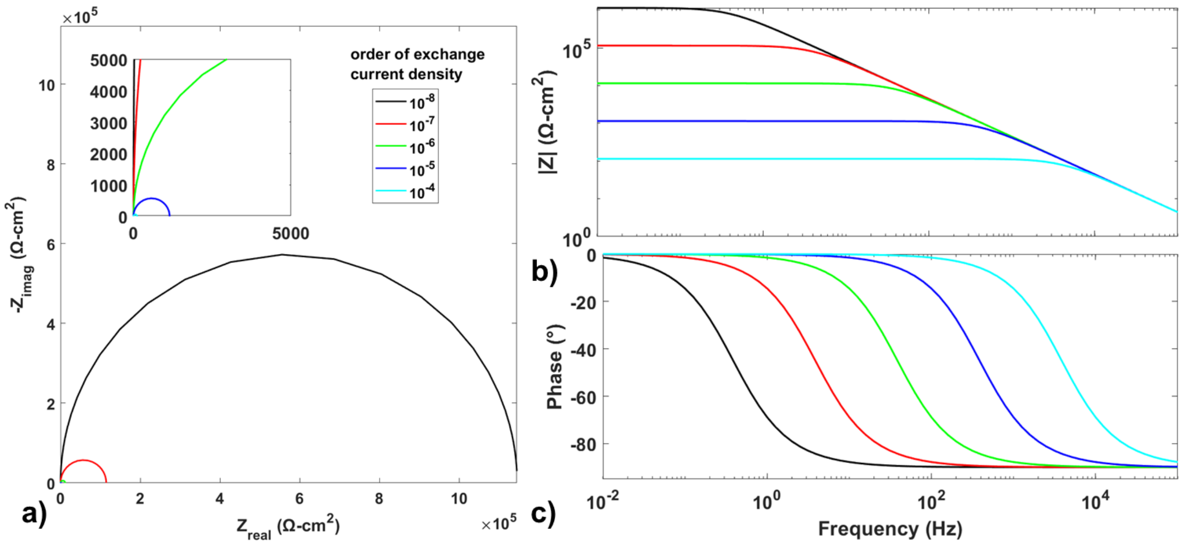

Figure 6: a) Nyquist, b) Bode, and c) Phase angle plots showing the role of exchange current density on the impedance response of the system

Results and Discussions

- <u>Task 1.1: Electrochemical Impedance Spectroscopy Study: Lab Data</u>

Figure 7 shows the effect of coating thickness on the impedance response of a coated substrate with two different holiday radii. For all coating thicknesses, there is little deviation in the impedance response between the three coatings for each holiday size. However, with the smaller holiday, the overall impedance response is larger than the samples with the larger holiday for all coating thicknesses.

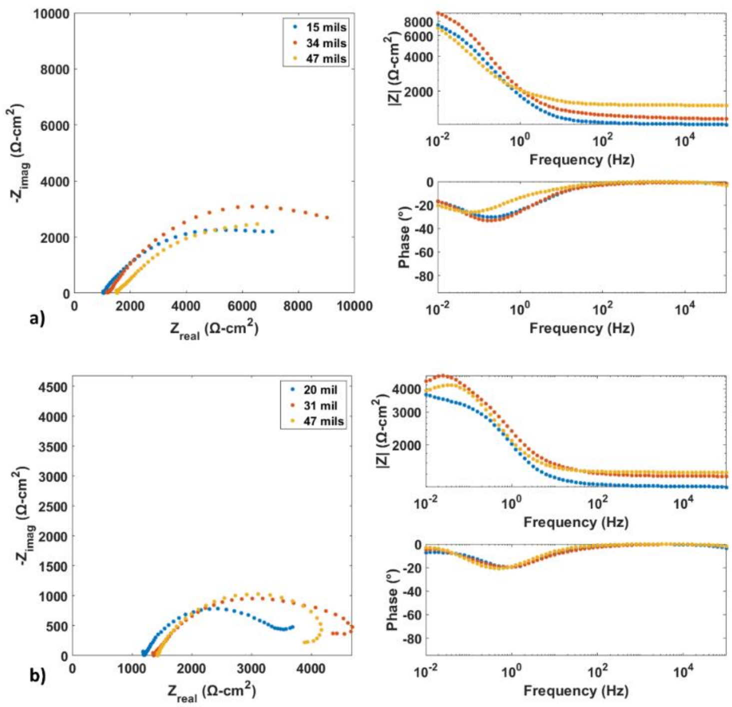

Figure 7: Effect of coating thickness on the impedance response of a coated substrate with a) 0.516 cm and b) 0.794 cm holiday

Figure 8 shows the effect of polarization conditions on the impedance response of FBE coatings with and without holidays present in the coating. At all potential values, intact coating shows consistently high impedance (10^{10}-10^{12} Ω-cm²) at low frequencies, with a linear decrease as frequency increases. This indicates excellent barrier properties and capacitive behavior characteristic of an undamaged coating. This is a characteristic response of the highly capacitive coating. The large and small holiday defects display much lower impedance values, by the large drop in overall impedance values and more positive phase angle values. Small holidays consistently show higher impedance values than large holidays across all protection potentials, suggesting better residual protection capabilities. As for the protection potential effect, OCP shows baseline behavior, whereas standard protection provides optimal results for defect mitigation. Both defect sizes show distinctive phase angle peaks in the mid-frequency range (10^0-10^2 Hz) when tested at OCP. For under protection, small holiday shows deeper phase angle minima (-40°) and large holidays exhibit shallower phase angle response (-20°). Under standard protection, phase angle minima become more pronounced for both defect sizes. Small holidays show more negative phase angles than large holidays. For over protection, phase angles become less negative and there is a convergence of phase response between large and small holidays. This reduction in phase angle variation shows more resistive behavior

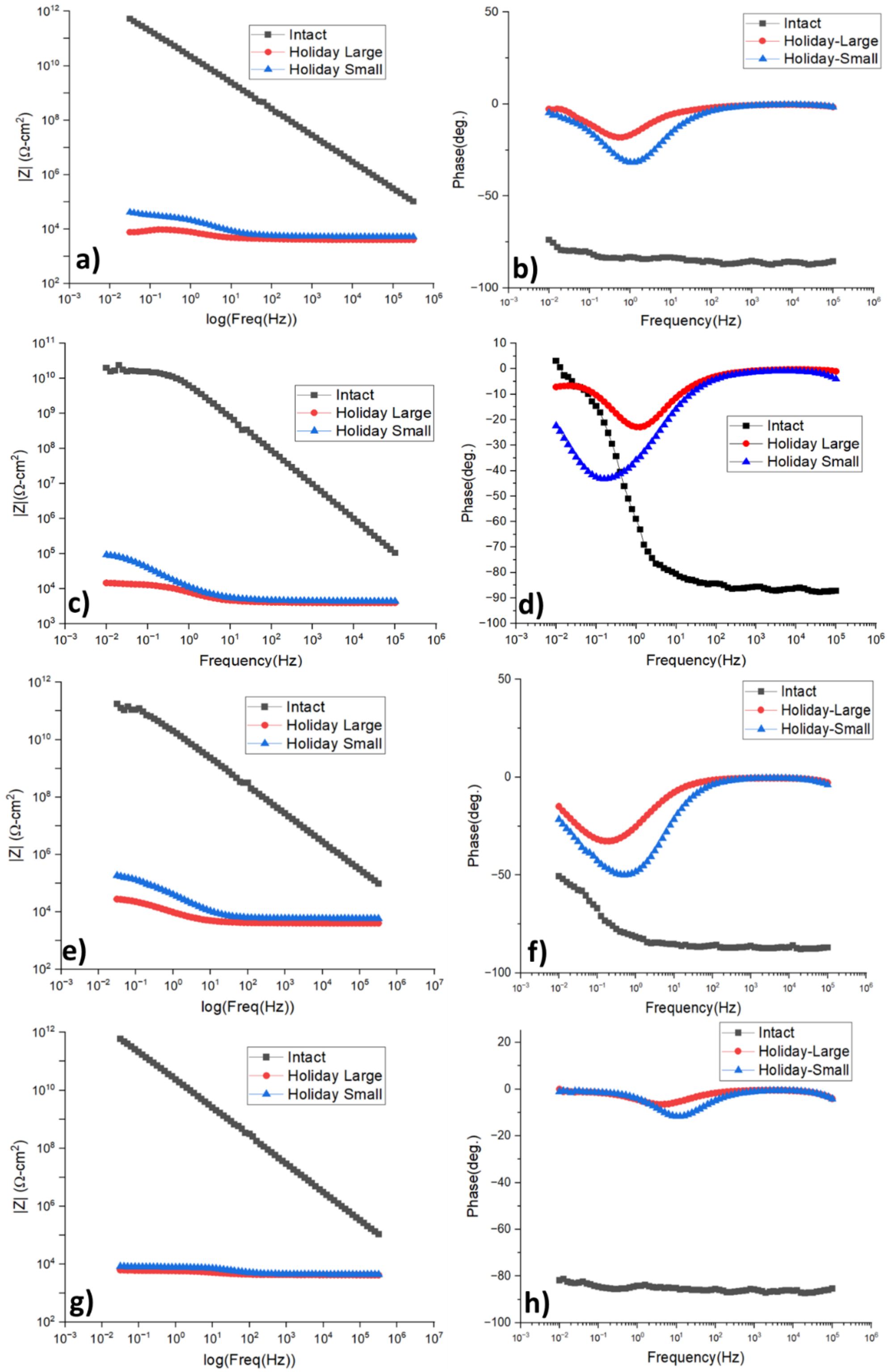

Figure 8: Bode and phase angle plots for FBE coatings with and without holidays for various CP conditions (a-b) open circuit conditions, (c-d) under protection, (e-f) standard protection, and (g-h) over protection

Figure 9 shows the effect of polarization condition on the impedance response of coal tar coatings with and without holidays present in the coating. The intact coating shown consistently high impedance (10^{10}-10^{12} Ω-cm^2) at low frequencies similar to FBE. These high values were shown for each polarization condition as well. The phase angle behavior for intact coating exhibits near-capacitive behavior approaching -90° and shows minimal frequency dependence in mid to high frequency ranges Defect responses in coal tar show clearer separation between the intact and damaged coating conditions. Applying the under protection potential for the coal tar coating defects did not produce drastic change from the OCP conditions. But, applying standard protection did increase the overall impedance relative to under protection potential and OCP conditions. For the over protection potential the overall impedance did drop but is most likely due to the higher rate of cathodic reaction occurring with the larger more negative potential that was applied to the surface.

The overall impedance response was very similar for the two coatings when various cathodic protection potentials were applied. The intact coatings showed large impedance values and phase angle values near -90° for most of the frequency domain regardless of the potential application. There was little difference between the impedance response between OCP and under-protection potential for FBE and coal tar coatings. This is most likely due to OCP and under-protection potential being similar in magnitude. Impedance measurements under the standard protection potential did show an increase in the impedance magnitude and more negative phase angle values for both small and large holidays. This is indicative that the exposed surface was more protected with the application of the standard protection potential. For both FBE and coal tar coatings when the over-protection potential was applied the impedance magnitude decreased and phase angle values became more positive. This is most likely due to the increased cathodic reaction rate with a more negative potential relative to the other three conditions.

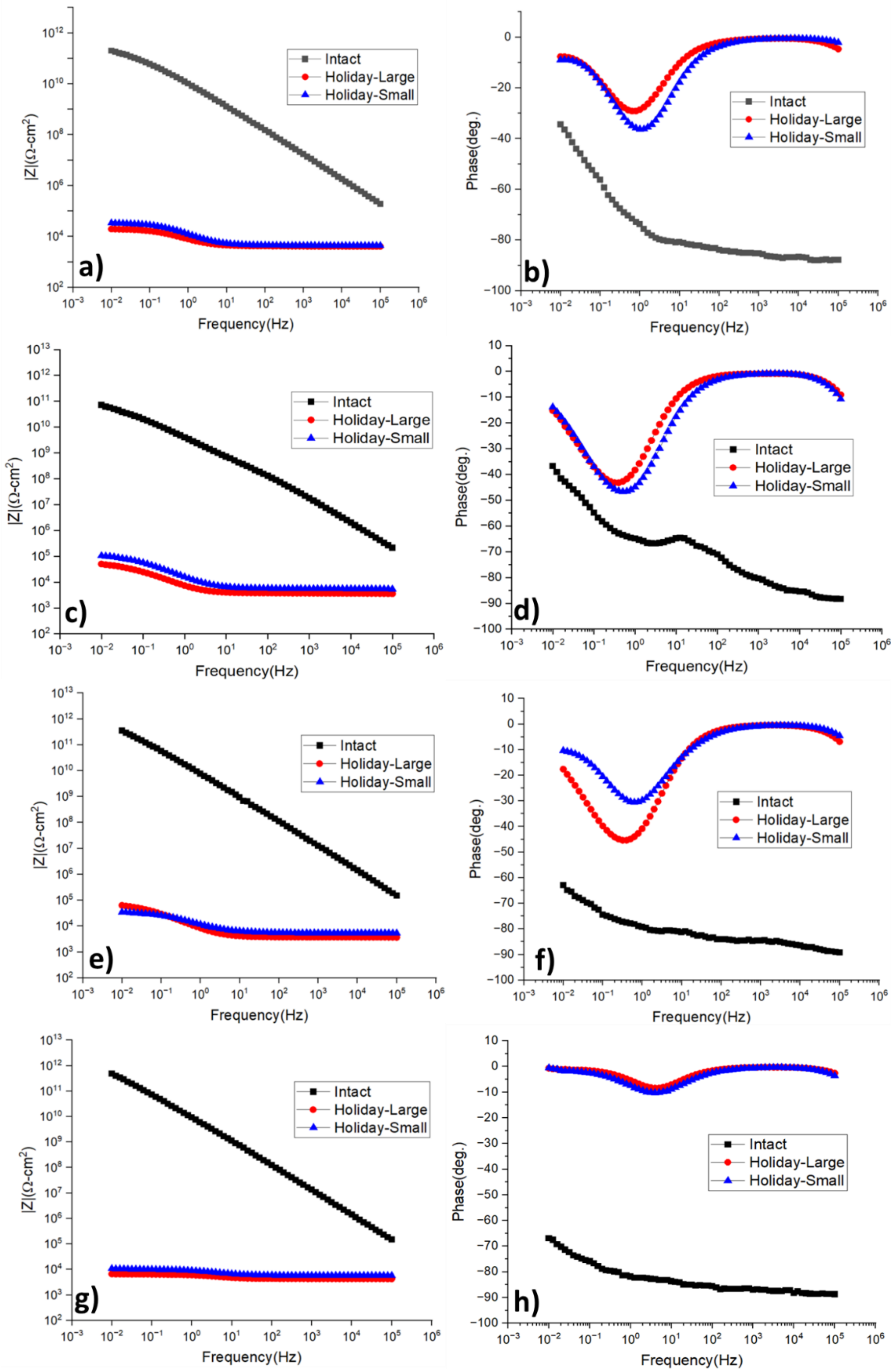

Figure 9: Bode and phase angle plots for Coal Tar coatings with and without holidays for various CP conditions (a-b) open circuit conditions, (c-d) under protection, (e-f) standard protection, and (g-h) over protection

References

1. Q. Zhao, V. Hautamaki and P. Fränt, "20 Q. Zhao, V. Hautamaki and P. Fränti, "Knee Point Detection in BIC for Detecting the Number of Clusters", ACIVS, 2008," in *International conference on advanced concepts for intelligent vision systems*, Berlin, 2008.
2. A. Kowalski, "The close interval potential survey (CIS/CIPS) method for detecting corrosion in underground pipelines," in *Underground pipeline corrosion*, Elsevier, 2014, pp. 227-246.

Project Financial Activities Incurred during the Reporting Period:

- The personnel from TAMU includes two PhD students, one full PhD student, one part-time PhD student, and one Master's degree student starting in June 2024. Two PhDs will perform task 1 and part of task 2. The Master's student will help to perform the testing methods. We added a new undergraduate student for testing and data analysis activities.
- The UDayton team includes Sreelakshmi Sreeharan as a PostDoc researcher in this project and continues her efforts in Task 2 and Task 3.
- No financial activities related to conferences or related activities.
- The laboratory has continued to increase the number of setups and measurements. The simulation of buried conditions will require more budget for Laboratory work and accessories. During the Laboratory work, we will perform different high-resolution characterization tools.

Financial Summary

- Federal Cost Activities:

  Total Direct costs: $93,184.03

  Total Indirect:33,841.54

  Total: $127,025

- Cost Share Activities:
  - Cost share contribution:

- Heuristech has contributed $24,400 in technology training and/or company personnel hours for physical laboratory testing and training to the Reflectometry and TLM analysis.
- Integrity Solutions has contributed $9,500 in CP field data collection, and technical staff resources to collect, collate, evaluate, screen, database development, and attend workshops. IS will contribute to the project with the database, increasing the co-share provided.
- The University of Dayton has contributed $30,436 in cost share.

Project Activities with Cost Share Partners:

During the fifth quarter of this project, we met three times with the co-sharing partners; the following outcomes from the meeting were:

- Meetings for updates on the project and future technical discussions.
- The partners are facilitating the collection of databases needed in this project.
- We will organize a technical workshop with the team partners to get feedback on our proposal concept. We will include some students to train them in the pipeline subject.

Project Activities with External Partners:

- We will organize a technical workshop with the team partners to get feedback on our proposal concept. We will include operators and external partners for feedback.
- We will organize different courses for pipeline companies, one of the topics will be integrity and risk based on CP.

Potential Project Risks:

We could finalize the NDAs for acquiring the needed database during this fifth quarter. We will have a larger database for different RoWs in the USA, which will strengthen and validate our current proposed algorithm. There is no impact for the performance of this project. The actions are summarized in the following table:

Task Risk	Priority	Risk Description	Impact Summary	Response Strategy
Select different pipelines for indirect inspection Task 3	Medium to High	-Database representing the required conditions	Identification of database illustrating CP history and available CP survey and pipeline inspection data.	The team has two robust sets of field data to develop the framework. This latter will be used in the next set of data.

Future Project Work:

We anticipate following the proposed timeline with no current changes during the next months. We will follow the Gantt chart to mark the progress and future plans.

During the next 30, 60, and 90 days, we will perform task 1 activities. We will extend more activities in Task 1. Also, we will continue with Task 2's activities and start with task 3 for the next 30, 60 and 90 days.

Theoretical work, laboratory work, and current database analysis will be considered for the next quarter. The acquisition of new database is going to be selected and we will determine if will help in the algorithm.

The timeline and schedule for the project are in the Gantt chart.

Task/Subtask	Fiscal Year											
	2023	2024				2025			2025	2026	2026	2026
	Q4	Q1	Q2	Q3	Q4	Q1	Q2	Q3	Q4	Q1	Q2	Q3
Task 1: Designing and building the physical prototypes in laboratory conditions and deterministic modeling												
Task 2: Integrating field inspection, theoretical with experimental data by applying pattern recognition techniques relating the pipeline-coating-soil system with CP												
Task 3: Validation of the *a priori* framework with experimental and field conditions for characterization/modeling and Evaluation/Validation												
Task 4: Development and validation of the methodology for ECDA based on CP levels												

Deliverable Milestones are indicated in black*, in dark green is the extended activities.

Potential Impacts to Pipeline Safety:

During the Transmission Line Modeling we integrate the algorithms used for Artificial Intelligence. The TLM will give more fundamental data with field and laboratory validation. The TLM was developed for multiscale conditions, the macro scale is validated with the field data (from Task 2). The micro conditions have been validated with Laboratory scale experiments (from Task1)
The potential impact is the results generated for the AI algorithm, the TLM is based on deterministic and fundamental approach. This can not only show different trends for a buried structure under cathodic protection but also include several features in the RoW. The rectifiers, anodic beds, soil compositions, current distribution, etc..

We are building an integrated algorithm not only based in data field but fundamentals.

Appendix

- Task 1.2: Fitting 2D TLM to the Lab data – Mechanistic Model

Figure 10 and Figure 11 displays the 2D TLM ability for using mechanistic definitions to fit data from an intact coating with various thickness and a 15-mil coating with a defect in the center of the exposed area. From Figure 10 it can be seen that the impedance response of the 2D TLM using mechanistic definitions for the coating capacitance was very similar to that of the experimental data. The difference between the model and experimental data is due to the model assuming a homogenous value of the coating thickness and ohmic resistance of the coating. Unlike the actual case there is a distribution of these across the interface which creates a deflection of the data from its ideal behavior. Overall the model was able to produce a similar impedance response that was seen in the intact coating case. The biggest deflection occurred in the thicker coating. This is most likely due to the thicker coating that was applied to the substrate, with thicker coating there is a more likely chance that the coating has some sort of defect that can influence the impedance response of the system. Also, with this first case of fitting the ohmic resistance of the coating was not changed from sample to sample in the 2D model but most likely there is some deviation of ohmic resistance between the actual coated samples that needs to be considered for a better fit. As of right now there is no model that is applied for determining the ohmic resistance of the coating, the value is just an assumed value in the 2D model.

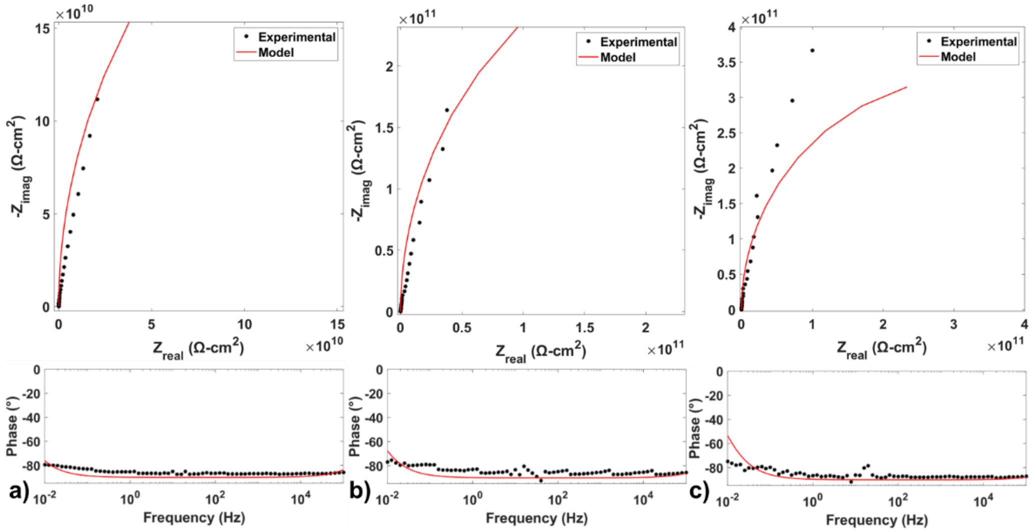

Figure 10: Nyquist and phase angle plots comparing experimental and model results for a) 15 mil, b) 25 mil, and c) 45 mil coatings.

Figure 11 shows the comparison of the 2D model with experimental results for a 15 mil FBE coating that had a holiday introduced into the coating exposing the substrate. Two initial measurements were performed on two separate locations and this data was used to check the validity of the model's output. From Figure 11 it can be seen that the 2D model was able to give a pretty good estimation of the general form of the impedance response of the system. The deviation between the model and experimental data is most likely due to the model assuming an idealized impedance response and assuming one time constant for the entire surface. In actuality there is a distribution of time constants in the experimental results that creates the deflection from idealized impedance response. To create a better fit of the model to experimental data it must be assumed in the model that there is some distribution of time constants.

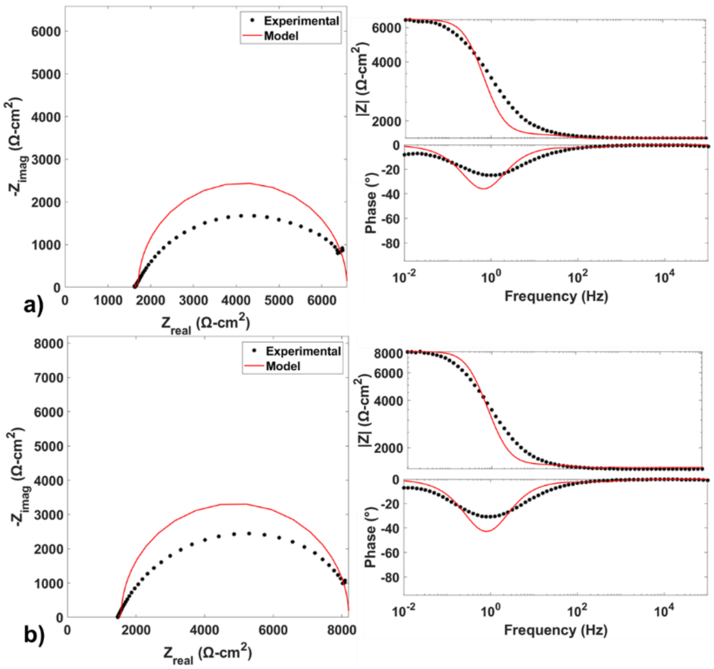

Figure 11: Nyquist, Bode, and Phase angle plots of a two different 15 mil FBE coating with a defect with an area of 0.275 cm^2

- Task 1.3: Potential decay Experimental Result

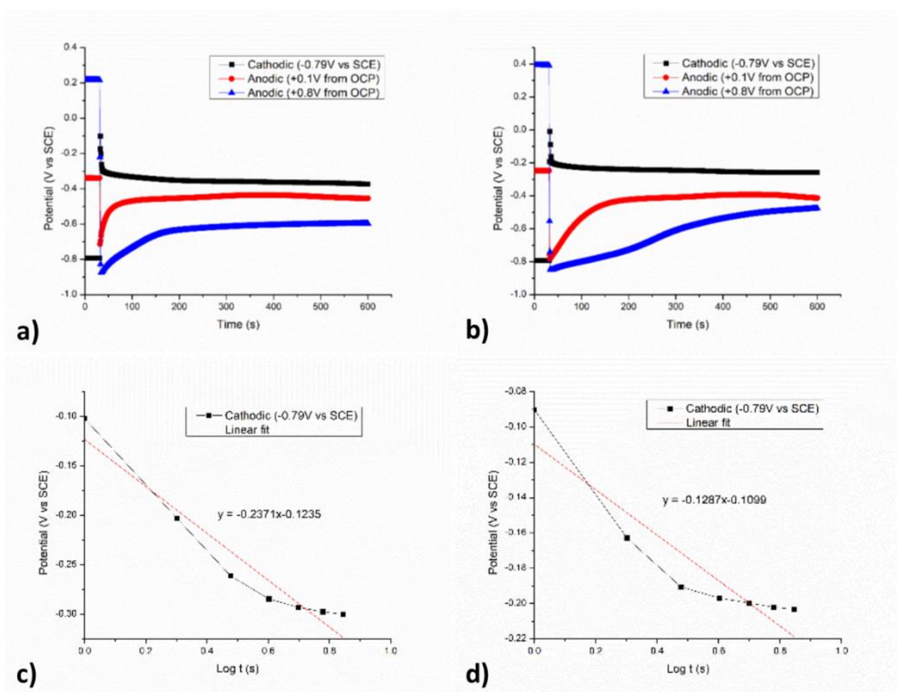

Figure 12: Potential decay versus time plots for a) FBE and b) Coal Tar coatings and Potential decay versus log(time) plots for c) FBE and d) Coal Tar coatings

Error! Reference source not found. Figure 12 show the potential decay versus time for all potential applications and log(time) under cathodic polarization. The cathodic condition at (-

0.79V vs SCE) exhibited the highest decay slope, followed by the anodic condition at (+0.1V from OCP). The lowest decay slope was observed under the anodic condition at (+0.8V from OCP). Overall, the decay's slope of fusion bonded epoxy (FBE) coating tends to be higher than the coal tar coating. But these cannot lead to any conclusion from this information because there a lot parameters need to be investigated during this thesis for example, Electrochemical Impedance Spectroscopy (EIS) need to be done to reveal the relation between the decay slope with impedance parameter. The absolute value of the potential decay slopes is shown in Table 3 for FBE and coal tar coatings respectfully.

Table 3: Potential Decay |Slope| (V/s) for FBE and Coal Tar coating

	FBE			Coal Tar		
	Cathodic	Anodic	Anodic	Cathodic	Anodic	Anodic
	-0.79 V vs SCE	+0.1V vs SCE	+0.8V vs SCE	-0.79 V vs SCE	+0.1V vs SCE	+0.8V vs SCE
1	0.2371	0.1257	0.0271	0.1039	0.0288	0.0069
2	0.1900	0.2380	0.0295	0.1420	0.0243	0.0059
3	0.1857	0.2361	0.0587	0.01287	0.0338	0.0093
AVG	0.2043	0.1999	0.0385	0.1249	0.0290	0.0074

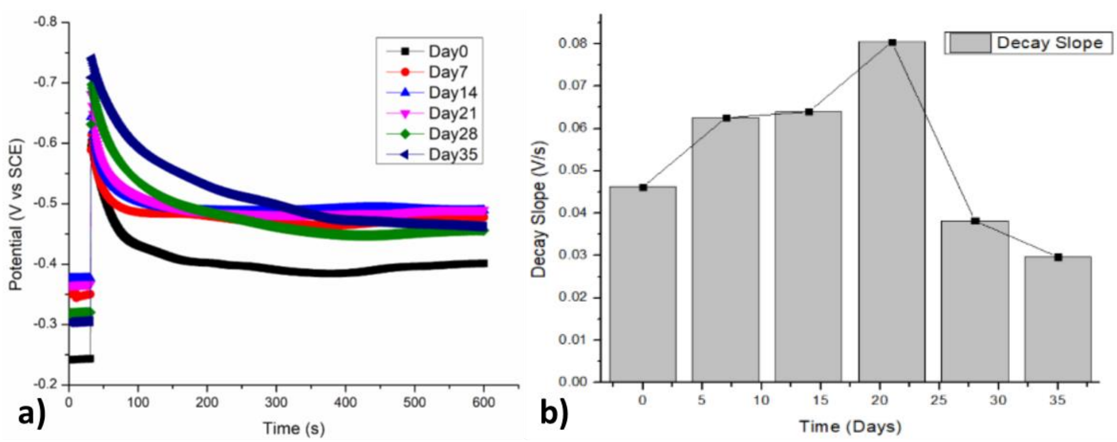

Figure 13: a) Potential Decay and b) Decay Slope for various immersion time

Figure 13 shows the potential decay and decay slopes for various immersion times for FBE coatings. Starting from Day 0, the decay slope was recorded at 0.0462 V/s. Over the following days, an upward trend was observed, with the decay slope gradually increasing, indicating a rise in the rate of degradation or coating deterioration. By Day 7, the decay slope rose to 0.0626 V/s, and by Day 14, it reached 0.0640 V/s. This upward trend continued, with the slope peaking at 0.0805 V/s on Day 21, marking the highest recorded decay rate. However, after Day 21, the trend reversed, and the decay slope began to decrease, suggesting a reduction in the degradation rate or a stabilization effect in the material or coating. On Day 28, the decay slope dropped to 0.0382 V/s, continuing this downward trend. By Day 35, the slope had further declined to 0.0297 V/s. This pattern, with an initial increase followed by a decrease in decay slope, might suggest that the sample initially absorbed the solution rapidly, causing an accelerated degradation, but later reached a phase where the absorption stabilized, reducing the rate of further degradation.

<u>Task 2 and Task 3</u>

A critical step in clustering analysis is determining the optimal number of clusters for a given dataset. Since clustering techniques rely on different data properties, various measures have been proposed to identify the best fit. For model-based clustering, the Approximate Weight of Evidence Criterion (AWE) is often used. When the Expectation-Maximization (EM) algorithm is employed to estimate the maximum likelihood of a mixture model, an approximation to AWE known as the Bayesian Information Criterion (BIC) is applicable. The BIC is given by

$$\mathrm{BIC} = 2\mathrm{loglike}(\mathbf{x}, \theta) - \mathrm{M}\log(\mathrm{n}) \qquad (7)$$

where, $\mathrm{loglike}(\mathbf{x}, \theta)$is the maximized log-likelihood, M is the number of independent parameters to be estimated, and n is the number of data points. A higher BIC value indicates a better model. This is because a well-fitting model yields a higher log-likelihood, while minimizing the number of parameters(M). Using the selected features, the number of clusters was determined by assuming a *k*-component multivariate Gaussian mixture distribution. The number of clusters (*k*) was varied from 2 to 20, and the process was iterated 10 times. The results are shown in Figure 14. The knee point of the BIC curve, observed at *k = 2*, indicates the optimal number of clusters[1].

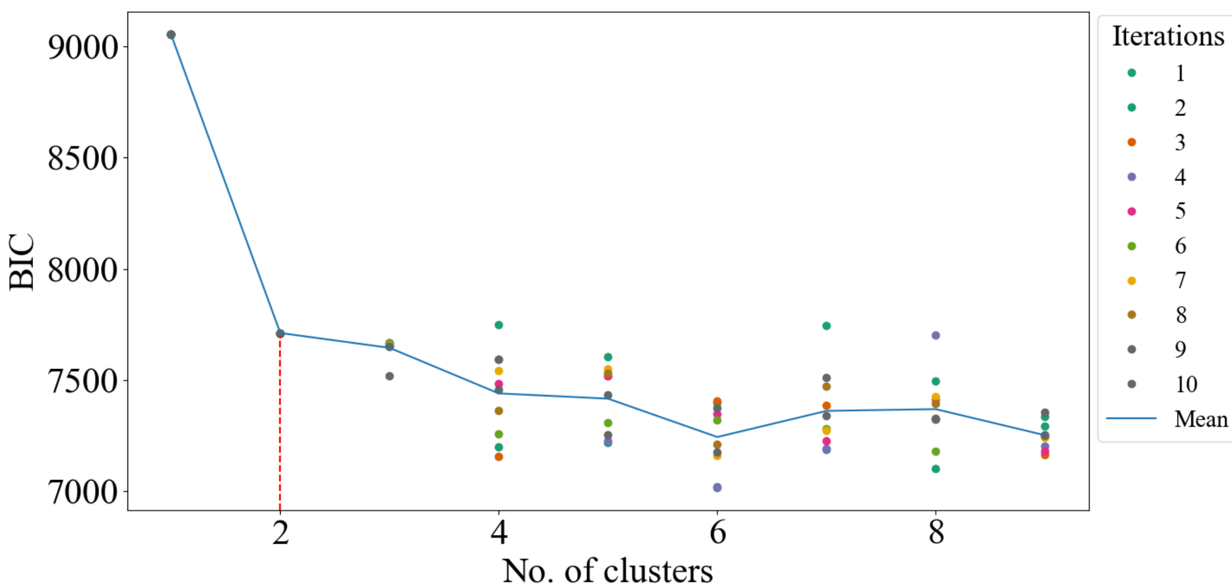

Figure 14: The number of components vs. BIC for full covariance structure, the vertical line indicates the possible optimal number of clusters.

An in-house Bayesian machine-learning algorithm was developed to infer model parameters based on the previously derived principal components and to perform unsupervised clustering analysis. The algorithm utilizes a probabilistic framework to account for uncertainties in the data and ensure robust clustering outcomes. The results of the clustering analysis are shown in Figure 15

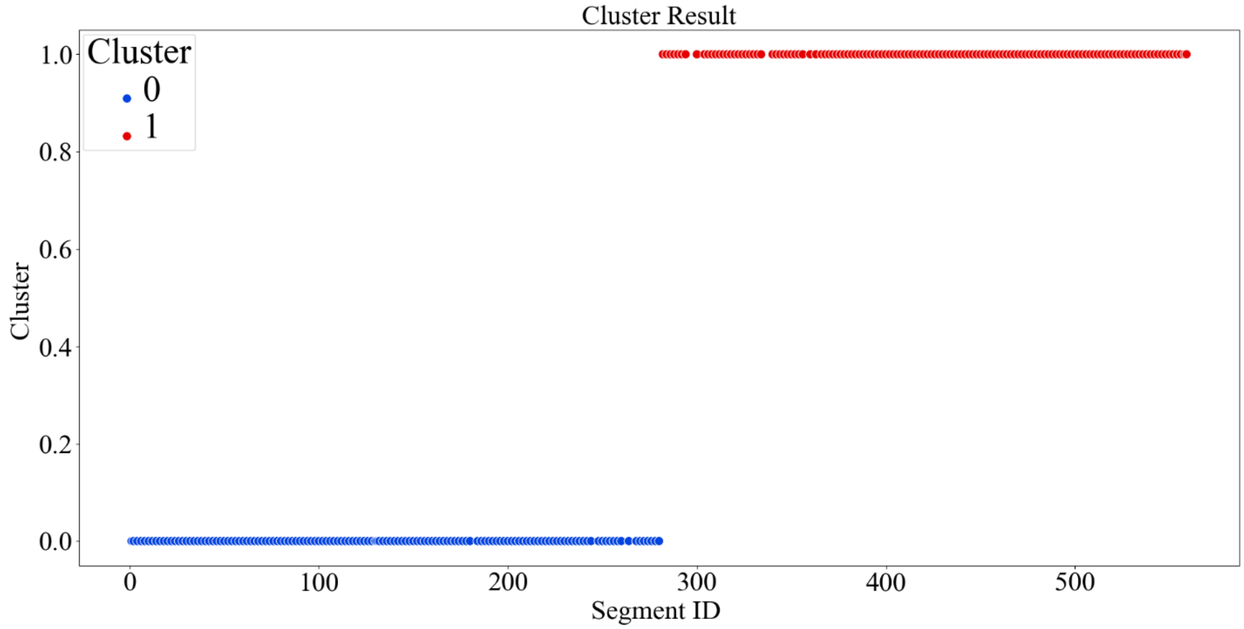

Figure 15: Clustering Results corresponding to k = 2

The clustering process begins with the Expectation-Maximization (EM) algorithm, which is used to extract statistical patterns, such as cluster centers and covariance matrices, from the dataset. This step enables the characterization of clusters based on their statistical behavior, including dispersion (spread) and sparsity (density). Figure 16(a) displays a 2D scatter plot of the first two principal components, with markers representing the cluster centers and contours outlining the Gaussian mixture distributions. The contours visually demonstrate the probabilistic boundaries of each cluster. Figure 16(b) presents a 3D scatter plot of the first three principal components, providing a more comprehensive visualization of the clusters. This plot highlights the separation between cluster groups more distinctly, confirming the effectiveness of the clustering algorithm in capturing the underlying structure of the data.

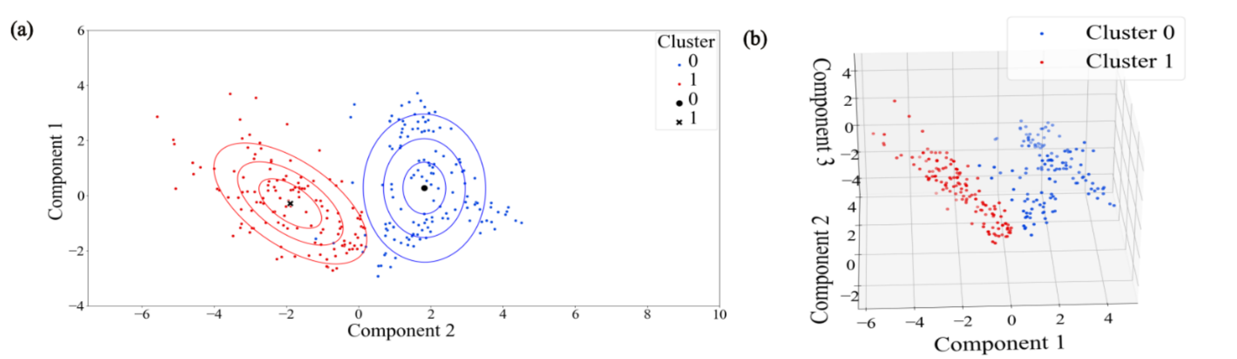

Figure 16: (a) Scatter plots of two principal components with centroid and contour for 2 clusters. (b) 3D scatter plots of three principal components.

This project aims to develop advanced methods for analyzing measured cathodic protection (CP) potentials. The CP potential data obtained from a close interval survey (CIS) for the specified region is visualized in Figure 17. Additionally, the metal loss depth, as estimated using an inline inspection (ILI) survey, is aligned with the CP potential data and overlaid for comparison. The analysis reveals a potential correlation between soil heterogeneity and regions of significant metal loss, highlighting the importance of understanding the relationship between soil properties and pipeline integrity.

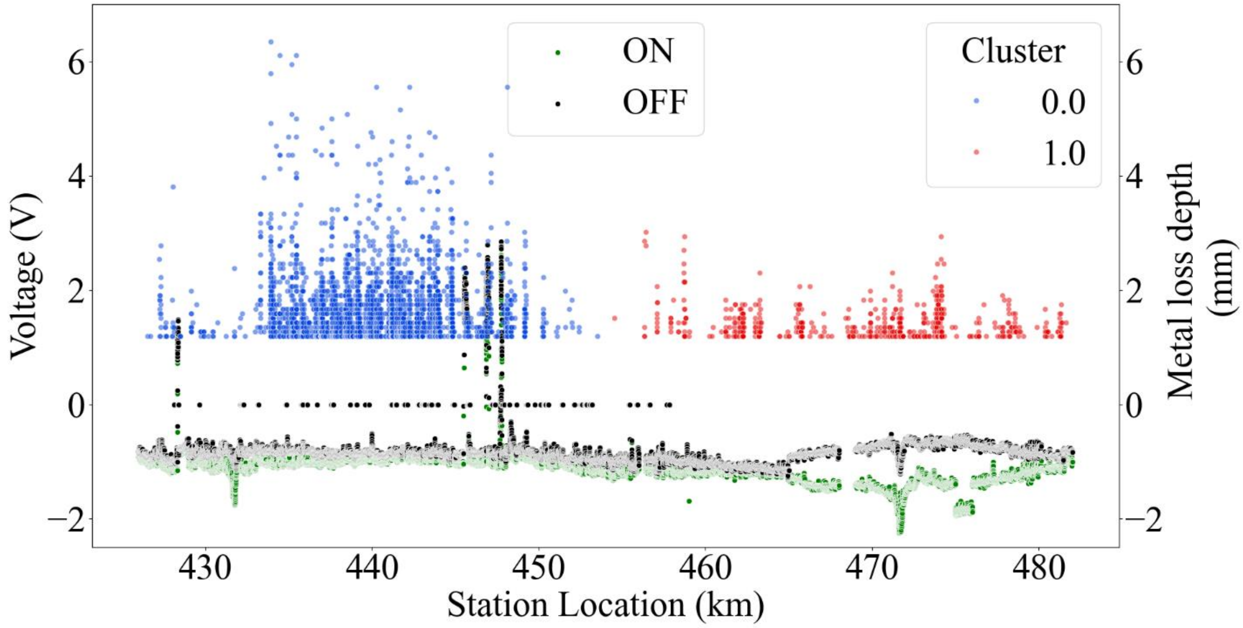

Figure 17: CP potential measured along the pipeline right of way aligned with ILI measured metal loss depth.

We begin the analysis of the CIS data by addressing the global trend caused by the influence of rectifiers and anodes. The potentials originating from the rectifiers exhibit an exponential decay with increasing distance from the source. Based on the data, the rectifiers are identified at 431.6467 km and 471.612 km, as highlighted in Figure 18(a). To prepare the data for analysis, outliers in the CIS measurements are first identified and removed. Subsequently, an exponential decay function is fitted to the rectifier locations to model the underlying global trend, as shown in Figure 18(b). This fitted trend represents the expected potential decay due to the rectifiers' influence. The trend is then subtracted from the CIS data to obtain the detrended data, which is presented in Figure 18(c). This detrending process isolates localized variations in the potential from the broader global influences[2].

To further analyze the detrended data, a wavelet transform is performed to generate a scale-location spectrogram. The scale is inversely proportional to frequency. Hence, this spectrogram provides a comprehensive view of how the signal's frequency content changes across different spatial locations. The wavelet transform decomposes the signal into its constituent frequency components while retaining spatial resolution, allowing the identification of localized features and variations. Figure 18(d) displays the resulting spectrogram, revealing prominent fluctuations in the signal.

These localized signal fluctuations will be further analyzed by focusing on smaller regions of interest and comparing them with physical pipeline features, such as valves, supports, and water crossings. This detailed examination aims to correlate signal anomalies with specific structural or environmental factors along the pipeline.

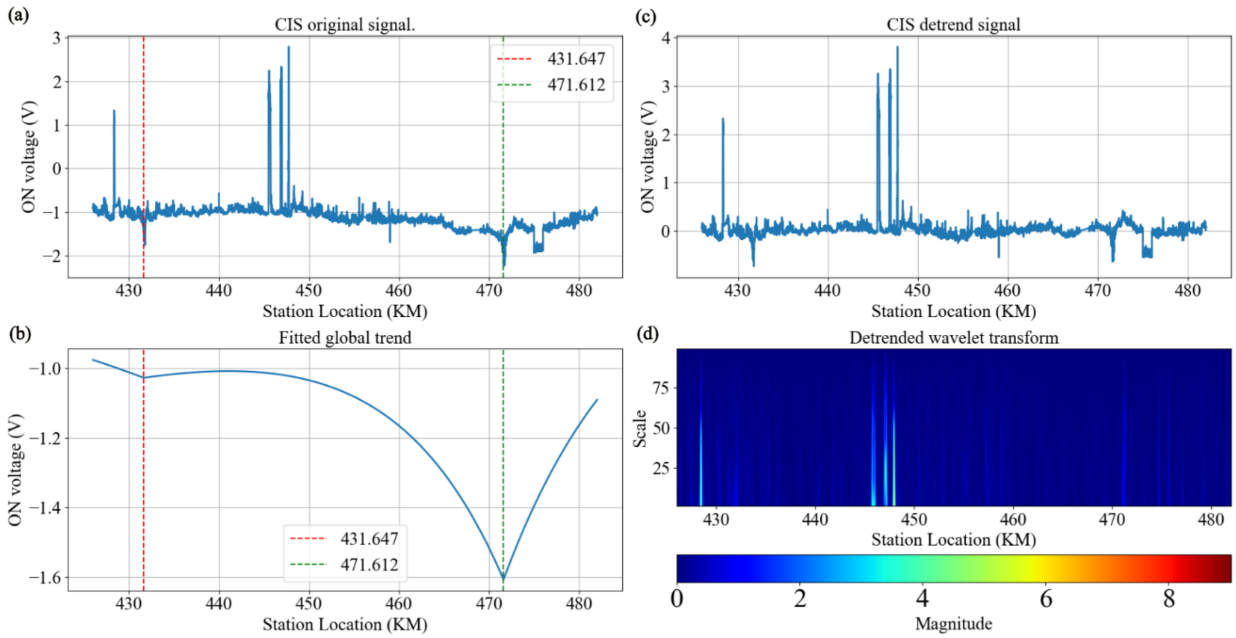

Figure 18: CIS on potential with location of rectifiers influencing the data. (b) Fitted global trend representing potential decay. (c) Detrended CIS data after removal of global trend and (d) Scale- location spectrogram from wavelet transform.

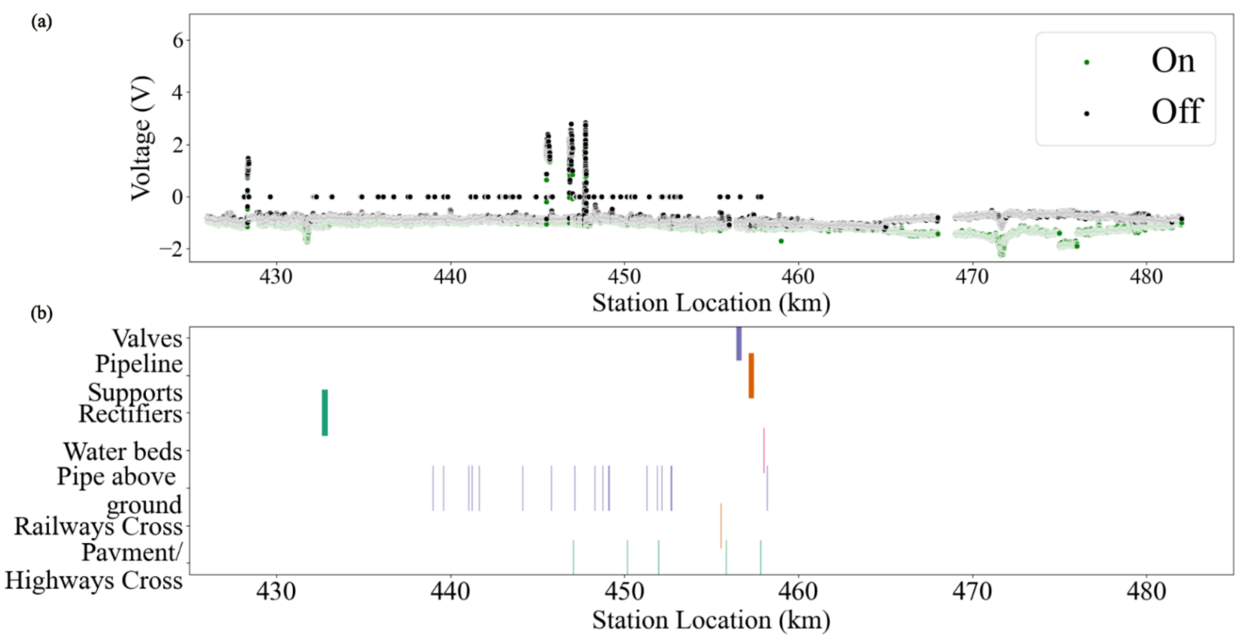

Figure 19: (a) CIS On and Off potential (b) Aligned pipe features